Research article

A novel simulation methodology for orthogonal cryogenic machining with CFD spray cooling integration

M. Pelosin [a],[*], P. Albertelli [a], T. Lucchini [b]

[a] *Dipartimento di Meccanica, Politecnico di Milano, Via Privata Giuseppe La Masa 1, Milano, 20156, Italy*
[b] *Dipartimento di Energia, Politecnico di Milano, via Lambruschini 4, Milano, 20156, Italy*

A B S T R A C T

The performance of cryogenic machining depends on the effectiveness of the heat transfer between the coolant jet and the chip in the cutting area because it affects the material temperature and the mechanical properties of the chip. This is a complex multi-physics problem because the solid deformation depends on the thermal and fluid–dynamic interaction with the cryogenic droplets generated by the atomization of the coolant jet. Within this context, this work applies an innovative methodology based on computational fluid dynamics to simulate the cutting process accounting for the interaction with the cryogenic jet. The proposed approach does not require empirical correlations since it integrates a predictive machining analytical model with Conjugate Heat Transfer CFD simulation and spray modelling to accurately estimate the heat transfer process accounting for the cooling effect of the impinging droplets. Complete Ti6Al4V dry and cryogenic cooled orthogonal cutting simulations were performed and results were compared with literature experimental data and state-of-the-art Finite Element Modelling simulations. The proposed methodology correctly estimates the cutting forces to vary cutting velocity and depth. Average errors in the resultant force estimation are 11.85% in dry and 14.4% in cryogenic cutting. Moreover, the experimental increase of the cutting force due to cooling is better estimated by the proposed approach with respect to FEM simulations. Thanks to the results accuracy and reduced computational costs, the proposed methodology could improve the understanding and the design of this innovative machining technology.

1. Introduction

Cryogenic machining takes the name from the type of fluid used as a lubricant in the cutting process, typically liquid nitrogen. It was developed to improve the machinability and the surface finish of hard-to-cut materials such as titanium alloys and to reduce the environmental impact of the machining sector.

The evaporation of oil-based cutting fluids produces toxic fumes harmful to the workers and the environment, and thus they require filtration and disposal systems. Switching to cryogenic fluids such as LN2 helps to reduce the environmental impact of the machining sector, as shown by the life cycle analysis performed by Damir et al. [1].

The employment of cryogenic fluid enhances the heat transfer during the cutting, reducing the thermal stresses and the wear. The chip formation mechanism differs from dry cutting as a consequence, as studied by Jianming Li et al. for cutting Ti6Al4V with localized supply of liquid nitrogen [2]. It was experimentally proved that this technology improved the overall performance compared to conventional cutting for a wide range of alloys [3]. The technology was also tested on

Polydimethylsiloxane (PDMS), a silicone polymer. Reducing the cutting temperature allows to keep this material below the glass transition condition, preventing it from converting into a rigid state. Albertelli et al. predicted a reduction of 22% in average of the process forces due to cryogenic cooling in milling of Ti6Al4V alloys [4]. Pereira et al. proved that internal CryoMQL improves tool life by 57% in comparison with emulsion coolant for milling operations [5]. It must be noted that the reduction of forces in cryogenic conditions is not trivial. Nalbant et al. noted an increase of cutting forces in cryogenic milling of AISI 304 to dry milling [6], the same behaviour was found in cryogenic orthogonal cutting of Ti6Al4V [7].

Different authors focused on the cooling abilities of cryogenic fluids. Pusavec et al. analysed the differences of the cooling performance between lCO2 and lN2 [8], a hybrid/experimental methodology for the heat transfer quantification of LN2 was proposed by Leqquien et al. [9]. Golda et al. studied the effect of different inflow configurations on the cooling performance [10].

Nomenclature

Abbreviation

CFD	Computational Fluid Dynamics
CHT	Conjugate Heat Transfer
FEM	Finite Element Modelling
HTC	Heat Transfer Coefficient
PSZ	Primary Shear Zone
SSZ	Secondary Shear Zone

Chip Curl Model

h	tool-chip interface length
r	Curl Radius
s	Inter lamellae spacing

Cutting Parameter

α	Rake Angle
f_r	Feed Rate
V_c	Cutting Velocity
w	Cutting width

Cutting Forces

F	Friction Force
F_c	Cutting Force
F_s	Shear Force
F_t	Thrust Force
N	Normal Force
R	Resultant Force

Predictive Model

ΔT_c	Average temperature rise
ΔT_m	Maximum temperature rise
ΔT_{cryo}	Cryogenic Cooling
$\dot{\gamma}$	Shear deformation rate
λ	Friction Angle
ϕ	Shear Angle
τ_{int}	Toll-chip shear stress
C_p	Heat Capacity
k_{AB}	Primary Shear Flow Stress
k_{int}	Toll-chip Shear flow stress
Q_{PSZ}	Heat dissipated PSZ
Q_{SSZ}	Heat dissipated SSZ
t_u	Uncut chip thickness
w	Workpiece width

Cryogenic Spray

ϵ	Heat Transfer Effectiveness
η	Disturbance
ω_b	Bubble growing rate
A_{wet}	Wetting Area
d_n	Surface Normal Distance
G	Vaporization Rate
k	Thermal Conductivity
k_b	Disturbance Fitting Parameter
m_d	Droplet Mass
q_a''	Air Heat Flux
q_d''	Droplet Heat Flux

q_s''	Solid Heat Flux
R_0	Droplet radius
R_i	Bubble radius
T_l	Liquid Temperature
T_w	Solid surface temperature
T_{sat}	Saturation Temperature
We	Weber number

Viscosity Model

$\dot{\bar{\epsilon}}$	Second invariant of the strain-rate tens
μ	Dynamic Viscosity
τ_Y	Tangential Yield stress

The characteristics of the cryogenic jet were numerically analysed by different researchers. The Volume Of Fluid approach was mainly used, however, these works were pure fluid–dynamic and they did not include the thermal energy contribution. The impact of the cooling jet on the tool surface was analysed by Salame [11]. Tahmasebi et al. analysed both the fluid behaviour inside the cooling delivery system and in the cutting zone of cryogenic milling [12].

The cutting process was numerically analysed by different authors. A numerical analytical model of end milling with internal cryogenic cooling was developed by Do Young Kim et al. [13]. A Finite Element Modelling (FEM) comparison of orthogonal cutting for dry and cryogenic machining was performed by Davoudinejad et al. [7].

The effect of the cryogenic cooling in these works was modelled by an estimation of the heat transfer coefficient on the work-piece and tool surfaces. For example, Pusavec et al. experimentally determined a heat function equation and than applied it to a orthogonal FEM simulation of INCONEL718 [14]. This approach is simple but has some limits linked to the complexity of the cryogenic impingement. The jet of the cryogenic fluid is affected by flash boiling. This phenomenon occurs when the environment pressure is below the saturation pressure of the liquid and it causes a drastic break-up. It sums up the classical aerodynamic break-up. Furthermore, the amount of heat exchanged by the fluid is a function of the impact angle with the solid surface and the droplets momentum. It follows that the average heat transfer is a function of the position of the fluid orifices and that a non-uniformity of the heat transfer exists on the solid surfaces. It is extremely difficult to introduce all these effects in a single analytic function, with the result that there is a large discrepancy between the heat exchange estimated by different functions. This complexity also implies that it is hard to know at priori the heat transfer characteristics of the available cooling system. Furthermore, the computational cost of FEM simulation is high, limiting their applicability to research.

A different approach to the analysis of the cutting process is the analytical modelling. A family of models based on the Oxley cutting theory was developed in this framework. These are derived from the application of the slip line theory to the cutting. They can estimate the cutting forces, the chip geometry and the heat generated by the orthogonal cutting process despite a negligible computational cost. Lalwani et al. extend Oxley's predictive cutting analytical model with the Johnson and Cook flow stress model [15]. This extension is useful since the Johnson and Cook flow stress model has become the standard for the description of the material behaviour for cutting simulations, extending the applicability to a wide range of cutting applications. Starting from Oxley theory, Bai et al. propose an analytical model of chip formation for precise prediction of orthogonal cutting of Ti6Al4V [16].

The modelling of the complete process, including the cooling jet can be achieved by coupling Computational Fluid Dynamics and a cutting simulation. Sprays have been extensively modelled and validated in the Computational Fluid Dynamics (CFD) framework. The modelling

approach more suitable for engineering applications is the Lagrangian framework [17]. It models the droplets as points with physical properties. In this framework, different sub-models have been developed to account for the droplet impingement on a solid surface and it is also possible to include a quantification of the heat exchanged.

Ideally, the coupling of a CFD solver for the cryogenic spray with a FEM solver for the cutting would give the best results. However, the implementation of such an approach will require auxiliary software to exchange information between FEM and CFD solvers. Moreover, the coupling of the two meshes is complex because they should be moved to accommodate the extreme deformations characterizing the chip. For these reasons, no works of this kind are present in literature, to the authors' knowledge.

This work proposes a novel simulation methodology based on the integration of analytic models for cutting and Conjugate Heat Transfer (CHT) CFD simulations to estimate the cutting forces, chip geometry and temperature map of cryogenic machining. This methodology allows an estimation of all the properties of interest for the cutting process, including the cutting forces, the chip geometry and a complete thermal map of both the chip and the tool.

Two alternative approaches are proposed for spray cooling: the classical one based on the definition of the heat transfer coefficient on the solid surfaces and the modelling of the cryogenic spray. The first approach is a fast tool to estimate all the properties of interest. The full description of the spray provides a more realistic modelling of the heat transfer in exchange for a larger computational time. The spray modelling can be also used a priori to estimate the heat transfer characteristics of a specific cooling system to impose in the following simulations.

The proposed methodology has been validated for different dry and cryogenic orthogonal cutting conditions of Ti6Al4V taken from literature [7]. The validation was performed against experimental data for forces and chip geometry and with FEM results for the thermal map. The cryogenic heat exchange was validated from heat transfer experimental data.

The results show that the simulation methodology proposed provides a good estimation of the cutting forces and geometry for both cases. The effect of the cryogenic jet on the forces is correctly captured. The derived temperature field is comparable to the one obtained with FEM simulation with a huge reduction of the computational time. Furthermore, the detailed description of the spray was used to estimate the heat transfer characteristics of a hypothetical cooling system. This analysis highlighted the non-uniformity of the heat transfer along the surfaces of the tool and the chip, which is not captured imposing the heat transfer on these surfaces. The effect of the non-uniformity on the temperature of the deformation zones was analysed by comparing the simulation with the spray with a second one imposing the average heat transfer coefficient derived by the post-processing of the first simulation. The result shows that the effect is small.

2. Methods

The following section describes the implemented simulation methodology. It begins with a general description of the framework. It is followed by a detailed description of all the models employed.

2.1. Simulation flowchart

Fig. 1 represents the framework of the methodology proposed. The analytical model takes the process information as an input:

- Tool geometry and properties: rake angle, density and heat capacity.
- Cutting conditions: Cutting velocity, uncut chip thickness, ambient temperature.
- Material property: density, heat capacity, thermal conductivity and Johnson Cook coefficients.
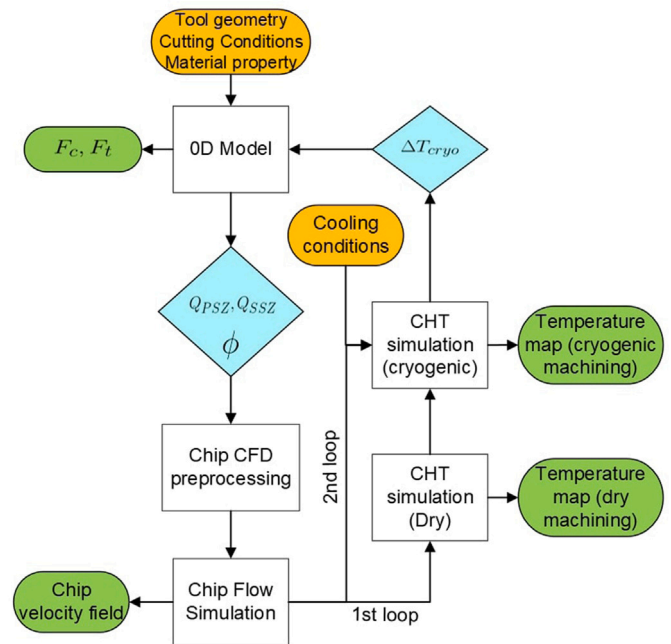

Fig. 1. Flowchart of predictive model for the cryogenic assisted orthogonal cutting.

The geometric outputs of this model (shear angle and uncut chip thickness) are employed to initialize the CFD domain and mesh of the chip. The CFD simulation is computed in a frozen-flow approach. Therefore, an adiabatic non-Newtonian flow simulation is run to impose the chip velocity field. The result is then used in the CHT thermal simulation. The dry and cooled cutting simulations are run and the temperature differences in the deformation regions between the two cooling conditions are calculated. The temperature estimation in the analytic model is corrected and both the cutting model and the cryogenic CFD simulation are run again to correctly estimate the forces, the geometry and the temperature map for cryogenic cutting. The temperature variation estimated in the deformation zones at the first iteration does not require further iteration to converge. The reason is that the heat propagates inside the chip for conduction and convection, it is therefore affected by the chip flow rate and the geometry. These quantities do not vary significantly among the first and second iterations, hence it is not necessary to evaluate again the effect of the cooling on the temperature. Cryogenic cooling can be modelled in the CFD simulation by imposing the Heat Transfer Coefficient (HTC) on the solid surfaces or simulating the spray. The predictive model was implemented in a Python script which interfaces with the OpenFoam software for the CFD simulations.

2.2. Predictive machining model

Predictive machining models provide a simplified description of the stress field of the cutting process. They are based on the Oxley theory [18]. It is a thick shear zone model which includes the effects of strain hardening, strain rate and temperature on the material properties. The most relevant assumptions of the theory are the following:

- Continuous chip formation, which implies steady-state conditions.
- Ideal Orthogonal cutting and plane-strain conditions.
- Ideal tool, no tool-tip radius.
- Both the primary shear plane (plane AB in Fig. 2) and tool-chip interface (plane BH) are considered as surfaces of maximum shear stress and strain rate.
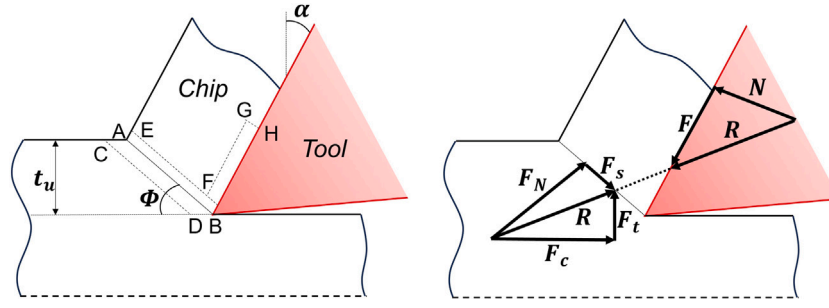
Fig. 2. Orthogonal cutting diagram.

The deformation of the chip occurs in the Primary Shear Zone (PSZ) (area CDEF in Fig. 2), which runs parallel and equidistant to the primary shear plane. Oxley's theory employs a power law formulation for the flow stress field. For this correlation, data are available in the literature only for low-carbon steel and a few aluminium alloys.

Lalwani [15] modified this theory to apply the Johnson Cook flow stress model Eq. (1) instead of a power law:

$$\sigma = (A + B\varepsilon^n)\left(1 + C\ln\frac{\dot{\varepsilon}}{\dot{\varepsilon}_0}\right)\left(1 - \left(\frac{T - T_w}{T_m - T_w}\right)^m\right), \tag{1}$$

where σ is the plastic flow field, ε is the strain, $\dot{\varepsilon}$ is the train rate, Tw is the wall temperature, T_m the melting points and A, B, C, n, m experimental coefficients. The effects of the material temperature and strain rate on the flow stress are hence considered. Furthermore, a large database exists for this flow stress model, making it applicable to a wider range of materials. Li et al. [19] generalized the Oxley's approach proposing the non-equidistant shear zone model. The primary shear zone is here divided into two regions: the wide entry region (CADB), and the narrow region (BAEF). The velocity change is slower in the wide region and higher in the narrow one. It follows that the main shear plane is no more in the middle of the shear region. This model was modified by Bai [16] to improve the prediction for orthogonal cutting of titanium alloys. The Bai model is detailed in the cited work, only the elements relevant to the analysis are presented and discussed.

The shear force (F_s) along the plane AB is proportional to the shear flow stress (k_{AB}), assuming a uniform stress distribution along the shear plane:

$$F_s = \frac{wt_u k_{AB}}{\sin\phi}, \tag{2}$$

where t_u is the uncut chip thickness, w is the width of the workpiece and ϕ the shear angle. The cutting and the thrust force can be therefore derived decomposing the shear force along the primary shear plane in the directions parallel and orthogonal to the cutting direction:

$$F_c = \frac{F_s}{\cos(\phi + \lambda - \alpha)}\cos(\lambda - \alpha), \tag{3}$$

$$F_t = \frac{F_s}{\cos(\phi + \lambda - \alpha)}\sin(\lambda - \alpha), \tag{4}$$

where λ is the friction angle and α the rake angle. The shear angle (ϕ) is computed using the Merchant formula and it is defined as the angle which minimizes the difference between shear stress at the tool-chip interface (τ_{int}) and shear flow stress (k_{int}) in the Secondary Shear Zone (SSZ) (area GHBF in Fig. 2).

The temperature in the PSZ and SSZ is computed to estimate the shear flow stresses. Bai estimates these temperature as:

$$\frac{dT}{dy_s} = \frac{\zeta\tau(y_s)\dot{\gamma}(y_s)}{\rho C_p V_c \sin(\phi)}, \tag{5}$$

$$T_{int} = T_{AB} + \psi\Delta T_M. \tag{6}$$

It follows that the temperature rise in the PSZ is the result of an integration of the shear power along this region, where τ is the shear flow,

$\dot{\gamma}$ is the shear deformation rate, ζ is the Taylor–Quinney coefficient, y_s is the local coordinate along the PSZ, and V_c the uncut chip velocity. ΔT_M is the maximum temperature rise in the chip occurring at the tool interface, this quantity is related to the average temperature rise in the chip ($\Delta T_c = FV_c/\rho V_c t_u w C_p$) by the Boothroyd equation [20]. This model was developed for dry machining, in the cryogenic case, the temperature rise in the deformation zones is reduced by the cooling effect. Two further terms are added to the temperature equations to account for the cooling, named dT_{cryoAB} and $\Delta T_{cryoInt}$. A similar approach was proposed by Do Young Kim in a cryogenic milling model [21].

$$\frac{dT}{dy_s} = \frac{\zeta\tau\dot{\gamma}}{\rho C_p V_c \sin(\phi)} - dT_{cryoAB}, \tag{7}$$

$$T_{int} = T_{AB} + \psi\Delta T_M - \Delta T_{cryoInt}. \tag{8}$$

Their value is quantified by the comparison between the dry and cooled CFD simulation in the first iteration of the methodology.

The heat generated in the primary and secondary shear zone is proportional to the energy required to deform the material. It follows that it can be computed as:

$$Q_{PSZ} = \int_0^{h_{PSZ}} dQ = \int_0^{h_{PSZ}} \rho C_p V\,dT = \int_0^{h_{PSZ}} \zeta\tau\dot{\gamma}\,dy_s, \tag{9}$$

in the primary shear zone, where h_{PSZ} is the length of the PSZ, computed according to the non-equidistant theory. The heat generated in the SSZ is computed as follows:

$$Q_{SSZ} = FV_c\frac{\sin\phi}{\cos(\phi - \alpha)}. \tag{10}$$

2.3. Chip curl estimation

The deformation of the chip and the friction along the tool-chip interface make it curve, also known as chip curling. This phenomenon is not considered by the hypothesis of the analytical cutting model employed. A simple model for the estimation of the curl radius was proposed by Horn [22]. This model is based on a geometrical derivation and defines the curl radius as:

$$r = \frac{t_u^2}{s\cos\alpha\sin\phi}, \tag{11}$$

where s is the inter lamellae spacing and t_u the uncut chip thickness. The lamellas are fine striations present on the free surface of the chip that are parallel to the cutting edge. This quantity was experimentally determined in the original work. However, it is possible to provide an approximation of its value as follows. The tool-chip interface is a function of s:

$$h = \frac{s \cdot t_u}{t_u - s\cos\alpha}, \tag{12}$$

assuming the tool chip interface as the one prescribed by the Oxley model, it can be expressed as:

$$h = \frac{\sin\theta \cdot t_u}{\sin\phi\cos\lambda}X, \tag{13}$$

with X function of other model parameters. The inter lamellae spacing is defined by combining the two equations in the framework of the analytical model, providing an estimation of the curl radius.
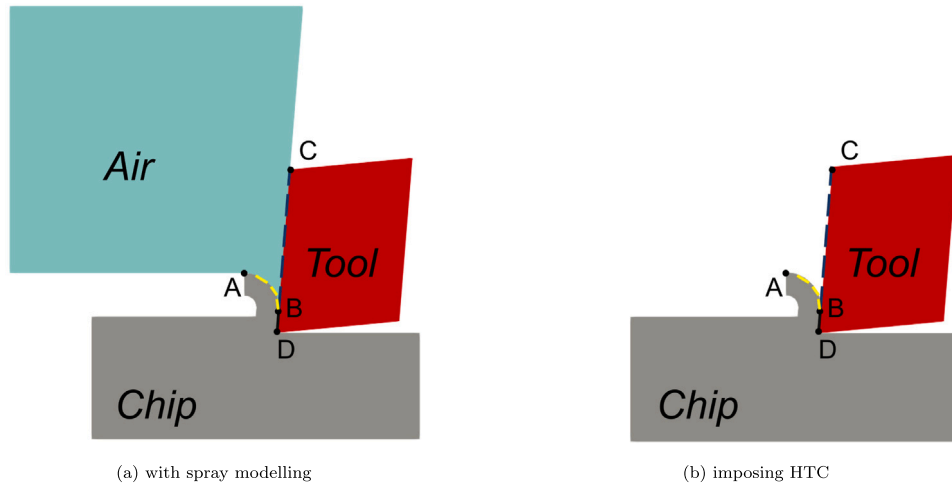
(a) with spray modelling   (b) imposing HTC

Fig. 3. CFD domain.

2.4. From analytical model to CFD simulation

CFD methodology is based on the Eulerian frame, hence fixing the volume of the analysis to a specific location. This approach can be employed in cutting simulation limiting the analysis to orthogonal continuous cutting. Since it is a steady-state process, the physical boundaries of the cutting region are therefore constant in time. It is hence possible to impose the geometry a priori and to simulate the flow in the domain. This approach was investigated in the past by different authors [23]. It is no longer used since it requires the knowledge a priori of the geometry, otherwise the achieved metal flow field is non-physical. An iterative procedure has the be set to converge to a physical solution. This limitation can be overcome thanks to the information derived from the cutting model. The geometry can be imposed starting from the computation of the shear angle and the curl radius by the cutting model. The physical flow field can be directly estimated without the necessity to iterate.

The flow of the work-piece metal can be modelled as rigid visco-plastic. In this particular type of non-Newtonian flow, the viscosity is a function of the flow conditions. The model for the viscosity employed in this analysis was proposed by Zienkiewicz [24]:

$$\mu = \frac{\tau_Y}{\dot{\bar{\varepsilon}}}, \tag{14}$$

where τ_Y is the tangential Yield stress and $\dot{\bar{\varepsilon}}$ is the second invariant of the strain-rate tensor. The viscosity tends to be infinite when no strain rate is present, the fluid hence behaves as a rigid material. When the flow is forced to turn by geometric constraints, the strain rate increases and the viscosity drops, allowing a rotation of the chip.

The heat generated during the cutting is introduced by a source term in the energy transport equation of the chip region. This term is non-zero only in the PSZ and SSZ, its magnitude is quantified as previously explained in Section 2.2.

2.5. CHT simulation for cryogenic machining

Once the model for the chip is set, it is possible to perform the Conjugate Heat Transfer simulation [25] in dry and cryogenic conditions. This type of analysis requires the simultaneous simulation of three regions: the air region, where the cryogenic spray eventually evolves, and two solid regions, the workpiece and the tool, as presented in Fig. 3.

The air and the spray exchange heat with the workpiece along the patch AB and with the tool along BC. The workpiece and the tool exchange heat along the patch BD. Depending on the condition analysed, the setup is different:

1. Dry cutting: the solids exchange heat with the air, all regions are hence simulated, Fig. 3(a).
2. Cryogenic cutting with spray modelling: the spray is simulated in the air region and the solids exchange heat with this region, Fig. 3(a).
3. Cryogenic cutting imposing boundary HT: air region is deactivated and a heat transfer coefficient is imposed on solid surfaces, Fig. 3(b).

An automated mesh strategy was developed to manage arbitrary tool configurations. The achieved mesh is fully hexahedral and the boundaries of the domain are computed based on the tool geometry, the cutting height and the procedure developed for the chip radius estimation Section 2.3. The cases without the spray modelling are treated as two-dimensional. This choice is consistent with the predictive machining model integration, which does not consider the gradients in the third dimension. Furthermore, the consequent reduction of the computational cost is useful to have a fast tool suitable for industrial applications. In the cases with the spray modelling a 3D set-up is performed since the spray cannot be represented in a planar 2D case. This was made by populating the third direction with cells and modifying the boundary conditions. In the 2D cases, the number of cells is the following: 11×10^3 for the workpiece, 3×10^3 for the air and 1×10^3 for the tool. For the 3D cases: 153×10^3 for the workpiece, 75×10^3 for the air and 7×10^3 for the tool. The time discretization adopted is first-order Eulerian, while the spatial discretization is limited second-order. The graphical post-processing of the CFD simulations is performed in *ParaView* [26], an open-source software for CFD post-processing.

2.6. Modelling of the cryogenic spray

The Eulerian–Lagrangian approach is used to model the dispersed phase (spray) which is described by computational *particles* representing a set of droplets with the same properties, for example: position, velocity, mass and temperature. The interaction with the continuous phase (air) equations is obtained by introducing source terms function of the point properties. The points can be considered as markers that are tracked in the continuous domain according to the implemented physics. The physics behind the evolution of the cooling spray and its interaction with the cutting region is complex. The breakup of the cryogenic jet at the exit of the nozzle is thermally driven and it takes the name of flash boiling. The interaction between the droplets and the solid surface follows under the so-called Leidenfrost interaction [27].

Flash boiling atomization is a catastrophic break-up of super-heated spray. This phenomenon is caused by the nucleation, growth and collapse of a vapour bubble inside the droplet. The breakup occurs

when the instabilities growing on the bubble–droplet interface exceed the characteristic length of the spray. The disturbance, η, grows with a rate ω_b, following the law:

$$\ln\left(\frac{\eta}{\eta_0}\right) = \int_0^t \omega_b \, dt \Longleftrightarrow \eta = \eta_0 \cdot \exp\left(\int_0^t \omega_b \, dt\right). \quad (15)$$

The characteristic length is assumed as the liquid film thickness, assumed as the difference between the droplet radius, $R_0(t)$, and the growing vapour bubble radius, $R_i(t)$. The initial disturbance, η_0 is assumed proportional the droplet radius, $\eta_0 = 0.05 R_0(t_0)$. Atomization hence occurs when:

$$\frac{\eta}{R_0(t) - R_i(t)} = k_b. \quad (16)$$

k_b is a fitting parameter to take into account the complexity of the phenomena. ω_b is the largest real root of the normalized growth rate equation, while the bubble growth rate was computed from the Rayleigh–Plesset equation, assuming spherical symmetry. To have a deeper explanation of the resolution of the break-up equation please refer to the following paper of Duronio et al. [28].

Flash boiling also affects the droplet vaporization rate ($G = dm_d/dt$), which is larger than the standard boiling regime. This contribution is modelled according to the work of Zuo et al. [29]. The total vaporization rate takes into account both the effect of conduction and convection with the surrounding gas and the contribution in the super-heat state (G_f) by a correlation proposed by Adachi:

$$G = 4 r_0 \pi \frac{k}{C_p} \frac{Nu}{1 + G_f/G} \ln\left[1 + \left(1 + \frac{G_f}{G}\right)\frac{h_\infty - h_b}{\Delta h}\right],$$
$$G_f = \frac{\alpha_s(T_l - T_{sat})A}{\Delta h}, \quad (17)$$
$$\alpha_s = C(T_l - T_{sat})^f.$$

Where h_∞ and h_b are the enthalpy of the gas in the gas mixture and at the drop surface respectively, Nu is the Nusselt number, m_d is the droplet mass and Δh is the latent heat of vaporization. k and C_p are the gaseous thermal conductivity and specific heat. C and f are constant dependent from the super-heat degree.

The type of interaction between the impinging droplets and the solid surface depends on both thermal and kinematic conditions. If the temperature of the surface is much larger than the saturation temperature of the liquid droplets, the high heat exchange at the impact causes the growth of a cushion of vapour at the interface. This vapour layer prevents the formation of a liquid wall film on the surface and reduces heat transfer. This type of interaction takes the name of Leidenfrost interaction. According to Kuhnke [30], it occurs when the temperature of the wall is at least 1.4 times bigger than the saturation temperature of the liquid. During the cutting, the heat produced by the deformation heats the chip above the ambient temperature. Since the saturation point of the nitrogen at ambient pressure is 77 K, the described interaction always occurs in the technology of interest.

An impingement model was hence developed. If a droplet is close to the wall, this model is applied to determine the post-interaction status (dynamic model) and the heat transfer (heat transfer model). The implemented methodology for the dynamic wall interaction is based on the Kuhnke model [30]. Depending on the impact velocity, the possible droplet interactions in the considered regime are a quasi-elastic rebound and a rebound associated with a breakup. The heat exchanged between the single droplet and the wall in the Leidenfrost regime is quantified by a semi-empirical correlation proposed by Deb [31], based on experimental measurements of the heat transfer of a stream of impinging droplets. The droplet heat transfer effectiveness (ϵ) is defined, which represents the ratio between the actual heat transferred with the wall and the total heat stored in the droplet (Eq. (18)):

$$\epsilon = \frac{Q_d}{m_d[\Delta h + C_{p,l}(T_{sat} - T_l)]}, \quad (18)$$

where $C_{p,l}$ the liquid heat capacity. The correlation proposed for the effectiveness is presented in Eq. (19):

$$\epsilon = 0.027 exp\left[\frac{0.08\sqrt{\ln(We_n/35 + 1)}}{(B + SF/60.5)^{1.5}}\right] + 0.21 K_d B exp\left[\frac{-90}{We_n + 1}\right]. \quad (19)$$

Where $We_n = \rho d U_{d,n}$ is the normal Weber number, $B = C_{p,v}(T_w - T_{sat})/\Delta h$ is the wall super-heat parameter, $K_d = k_v/(\mu_v C p_v)$ is the vapour parameter, $SF = e_s/e_{st} - 1$. is the surface material parameter, which is referenced to the steel thermal effusivity $e_{st} = \sqrt{k_{st} C p_{st} \rho_{st}}$.

2.7. Regions coupling

The thermal coupling between the chip-tool and fluid regions is made following the Conjugated Heat Transfer (CHT) framework. A custom boundary condition is implemented to solve the heat transfer problem at the interface. The heat flux on the surface of each solid boundary cell is composed of two different contributions: convective heat transfer with the gaseous region, and the heat exchanged between the solid and the droplet (Fig. 4).
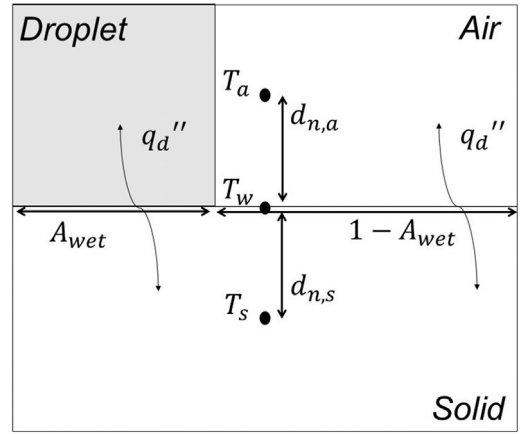

Fig. 4. Graphical illustration of developed boundary condition.

The proportion between these fluxes depends on the sum of the area occupied by the impinging droplets (A_{wet}). The heat transfer problem is formulated in Eq. (20):

$$\begin{cases} q_s'' = q_d'' & for \; A_{wet} \\ q_s'' = q_a'' & for \; 1 - A_{wet}. \end{cases} \quad (20)$$

Where q_d'' is the droplet heat flux computed according to the methodology explained in the previous Section 2.5, q_a'' is the convective heat flux
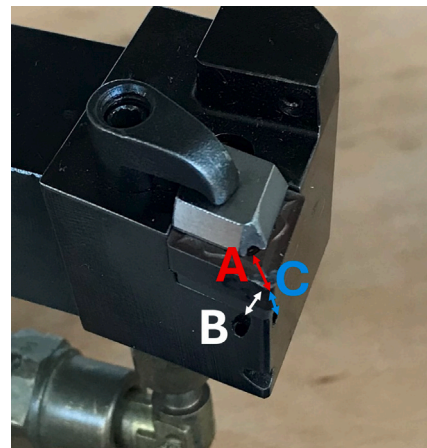

Fig. 5. Cryogenic tool.

exchanged with the air and q_s'' is the solid heat flux. The heat transfer problem is treated as a conduction problem, hence the Fourier law (Eq. (21)) is applied to quantify the heat exchanged across the surface:

$$\begin{cases} q_d'' &= -k_s \frac{\partial T}{\partial n}|_w & for\ A_{wet} \\ -k_a \frac{\partial T}{\partial n}|_w &= -k_s \frac{\partial T}{\partial n}|_w & for\ 1 - A_{wet}. \end{cases} \quad (21)$$

Where k_s is the thermal conductivity of the solid and k_a the effective thermal conductivity of the air, defined as the sum of a molecular and a turbulence contribution:

$$k_a = \frac{\nu}{Pr} + \frac{\nu_t}{Pr_t}, \quad (22)$$

with ν and ν_t molecular and turbulent kinematic viscosity and Pr and Pr_t molecular and turbulent Prandtl number. This definition allows to model the effects of the flow condition on the boundary heat transfer. The cell surface temperature equilibrium is the weighted average between the surface temperature below the droplet and the portion in equilibrium with the fluid (Eq. (23)):

$$T_w = A_{wet} T_{w,d} + (1 - A_{wet}) T_{w,a}. \quad (23)$$

The heat flux discretization is presented in Eq. (24):

$$\begin{cases} q_d'' &= -k_s(T_{w,d} - T_s)/d_{n,s} & for\ A_{wet} \\ -k_d(T_{w,a} - T_s)/d_{n,s} &= -k_a(T_{w,a} - T_a)/d_{n,a} & for\ 1 - A_{wet}, \end{cases} \quad (24)$$

where T_w is the surface temperature, T_s and T_a are the cell centre temperatures, while d_n is the normal distance between the cell centre and the boundary face centre. The averaged surface temperature can be computed by combining Eqs. (23) and (24). At each time step, the boundary condition corrects the temperatures of the air and the solid surfaces, the heat then diffuses by conduction within the domains. The coupling between solid regions is a simplified version of the one explained above and it reduces to:

$$\begin{cases} T_{w,1} &= T_{w,2} \\ -k_{s,1}(T_{w,1} - T_1)/d_{n,1} &= -k_{s,2}(T_{w,2} - T_2)/d_{n,2}. \end{cases} \quad (25)$$

3. Results

The validation of the proposed methodology follows different steps. The capability to capture the cutting forces and the chip geometry was tested against experimental data of orthogonal cutting of Ti6Al4V [7]. The achieved chip geometry, flow and temperature fields were compared to FEM simulations available in the same study. The cryogenic cutting was then analysed, initially with the classic approach and then introducing the full description of the spray. The temperature maps and the cutting forces are presented and the forces are compared with the experimental measurement and FEM results. The differences between the two approaches for the cryogenic cases are highlighted.

All machining tests were performed using a CNC Somab Unimab 400 lathe fitted with a Sandvik CNMG 120408 SMR1115 cutting insert, suited for machining titanium alloys. The LN2 supply system is composed by a dewar, a pressurized tank to store the nitrogen at saturated conditions. This vessel is connected to the tool-holder by an insulated pipe and a phase separator. The cooling configuration is based on three simultaneous injections, one on the rake and two on the flank faces (Fig. 5). The distance between the rake fluid hole (quote A in Fig. 5) and the cutting edge is 5.12 mm, and the two flank nozzle distances are 11 mm (quote B) and 10.2 mm (quote C).

3.1. Dry cutting

The cutting conditions analysed are summarized in Table 1.

Table 1
Cutting parameters.

Parameter	value
Rake Angle [°]	4.6
Flank Angle [°]	5.4
$V_{c,1,2}$ [m/min]	40, 50
$f_{r,1,2}$ [mm/rev]	0.2, 0.3
w [mm]	1.6

The Bai model optimized for Titanium alloys has been used. The parameters of the constitutive models for the materials have been kept equal to the ones used by the original authors. The results of the models are shown in Fig. 6 in terms of the cutting and thrust force and friction angle (λ), the error analysis is performed for both numerical approaches against the experimental measurement of the resultant of the forces.

The friction angle is connected to the friction coefficient (μ) at the tool-chip interface. It is the angle between the normal and the tangential component of the forces on the interface, following the definition of the friction coefficient:

$$\lambda = \tan^{-1}(\mu) = \tan^{-1}\left(\frac{N}{R}\right). \quad (26)$$

For the conservation of the forces, and applying trigonometrical consideration, the proportion of the cutting and thrust forces is also function of this angle:

$$\frac{F_t}{F_c} = \tan(\lambda - \alpha). \quad (27)$$

The primary shear angle (ϕ) is a function of the difference between the friction angle and the rake angle. In the model proposed by Moufki [32] employed in this work the correlation is the following:

$$\phi = A_1 + A_2(\alpha - \lambda), \quad (28)$$

with A_1 and A_2 material constants. Since the rake angle is imposed by the tool geometry, the friction angle is proportional to the shear angle. It can be used as a parameter representing the geometry of
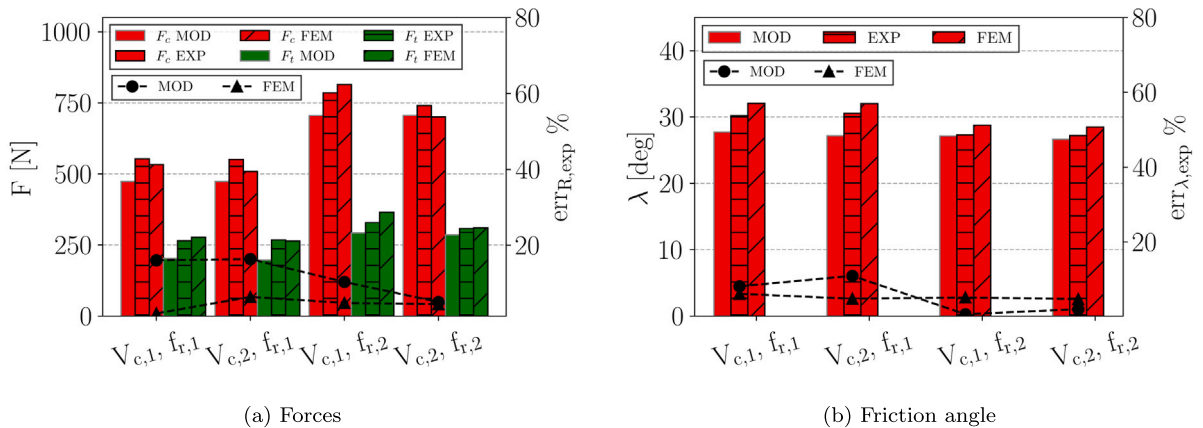

(a) Forces   (b) Friction angle

Fig. 6. Cutting and Thrust forces and friction angle for dry cutting conditions: numerical prediction vs experimental measurements vs FEM prediction.
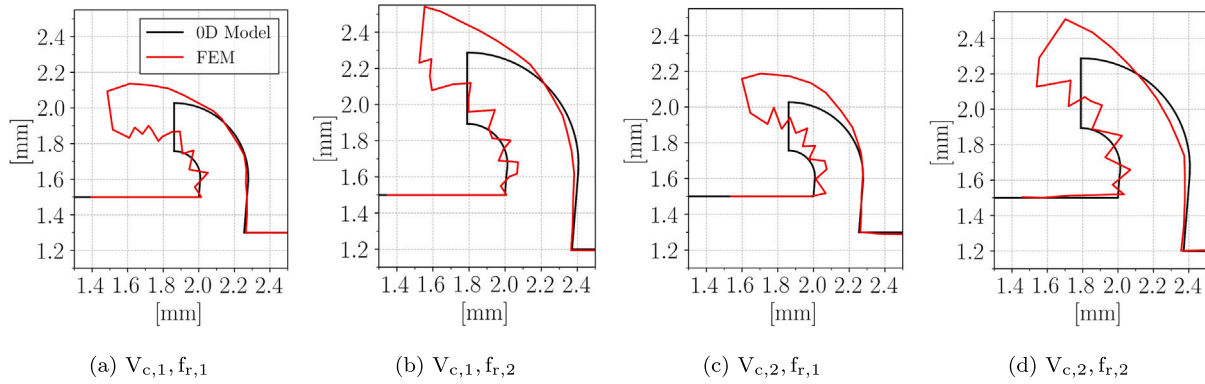
(a) $V_{c,1}, f_{r,1}$ (b) $V_{c,1}, f_{r,2}$ (c) $V_{c,2}, f_{r,1}$ (d) $V_{c,2}, f_{r,2}$

Fig. 7. Chip shape estimation for different Ti4Al6Av cutting conditions: numerical vs FEM prediction.

the chip. It follows that the experimental comparison of the friction angle (Fig. 6(b)), computed rearranging Eq. (27), shows the capability of the model to capture both the tool-chip friction and the primary shear angle. The analytical models estimate an overall resultant of the forces smaller than the experimental measurements (Fig. 6(a)). This behaviour is justified by the assumption of an ideal tool. Real tools are characterized by a tip radius, the stress applied to the material is therefore less concentrated and a higher force is required to deform and break the workpiece. The error analysis shows that the prediction of the resultant of the forces is better for higher cutting height. The error of the friction angle is comparable among the FEM and analytical model.

Fig. 7 shows the comparison between the boundary of the CFD domain obtained by using the shear angle and the chip curl radius from the analytical model and the boundary of the FEM simulations. The FEM predicts the segmentation of the chip, this phenomenon cannot be captured by the simulation methodology proposed. It could be however estimated a posteriori by a model proposed by Bai [16]. The prediction of the curl radius is close to the FEM one for the majority of the cases.

Fig. 8 shows the computed chip velocity and viscosity for a cutting condition taken as an example ($V_{c,1}, f_{r,1}$). The viscosity far from the deformation zones is extremely high, the flow motion is hence rigid. Approaching the deformation zones the flow is forced to turn. A decrease in the viscosity follows this deformation. This is necessary, otherwise the force required to make the flow turn would be infinite. The velocity in the deformed chip is slower than the not deformed region due to the increase in the crossing area. This type of flow field is physical and it is expected from the cutting theory since the deformation happens mainly along the primary shear zone.

The amount of heat dissipated in the deformation regions is presented in Table 2.

The power increases with the cutting velocity and the undeformed chip thickness. Fig. 9 shows the comparison between the temperature

Table 2
Heat produced in primary and secondary deformation zones.

	Q_{PSZ} [W]	Q_{SSZ} [W]
$V_{c,1}, f_{r,1}$	176.6	49.15
$V_{c,2}, f_{r,1}$	221.2	61.56
$V_{c,1}, f_{r,2}$	263.8	72.6
$V_{c,2}, f_{r,2}$	330.5	90.97

fields of the FEM and CFD approaches. The results are close in the slower cutting conditions. The cases with a higher velocity show an overestimation of the temperature. The temperature along the tool-chip interface is generally more uniform for the CFD results. The FEM prescribes a detachment of the chip very close to the tool edge. The heat produced by friction with the tool is hence limited to that region, concentrating and reducing the temperature rise.

3.2. Cryogenic cutting

The cryogenic cutting simulations are discussed in the following section. The classic approach is treated at first, followed by the modelling of the spray impingement. It must be noted that the cryogenic FEM simulation imposed a heat transfer coefficient equal to 2000 kW/(m²K) only to the rake face. According to the authors of the reference paper, this value is overestimated and it is used to rapidly reach the steady state conditions of temperature. It is our opinion that this approach distorts the heat flux of the problem and thus the temperature field. For this reason, no comparison of the temperature against FEM results is presented in this section.
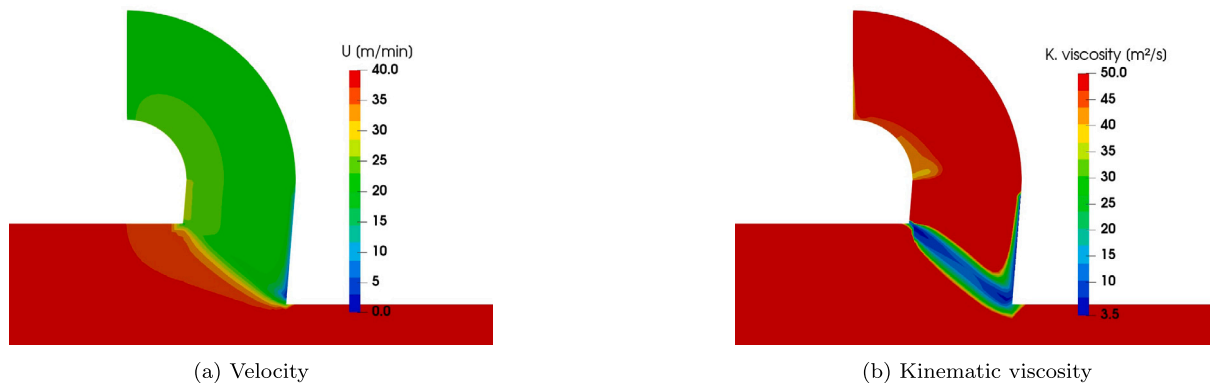

(a) Velocity   (b) Kinematic viscosity

Fig. 8. Chip velocity and viscosity ($V_{c,1}, f_{r,1}$): numerical prediction.

(a) $V_{c,1}, f_{r,1}$, FEM

(b) CFD Model

(c) $V_{c,2}, f_{r,1}$, FEM

(d) CFD Model

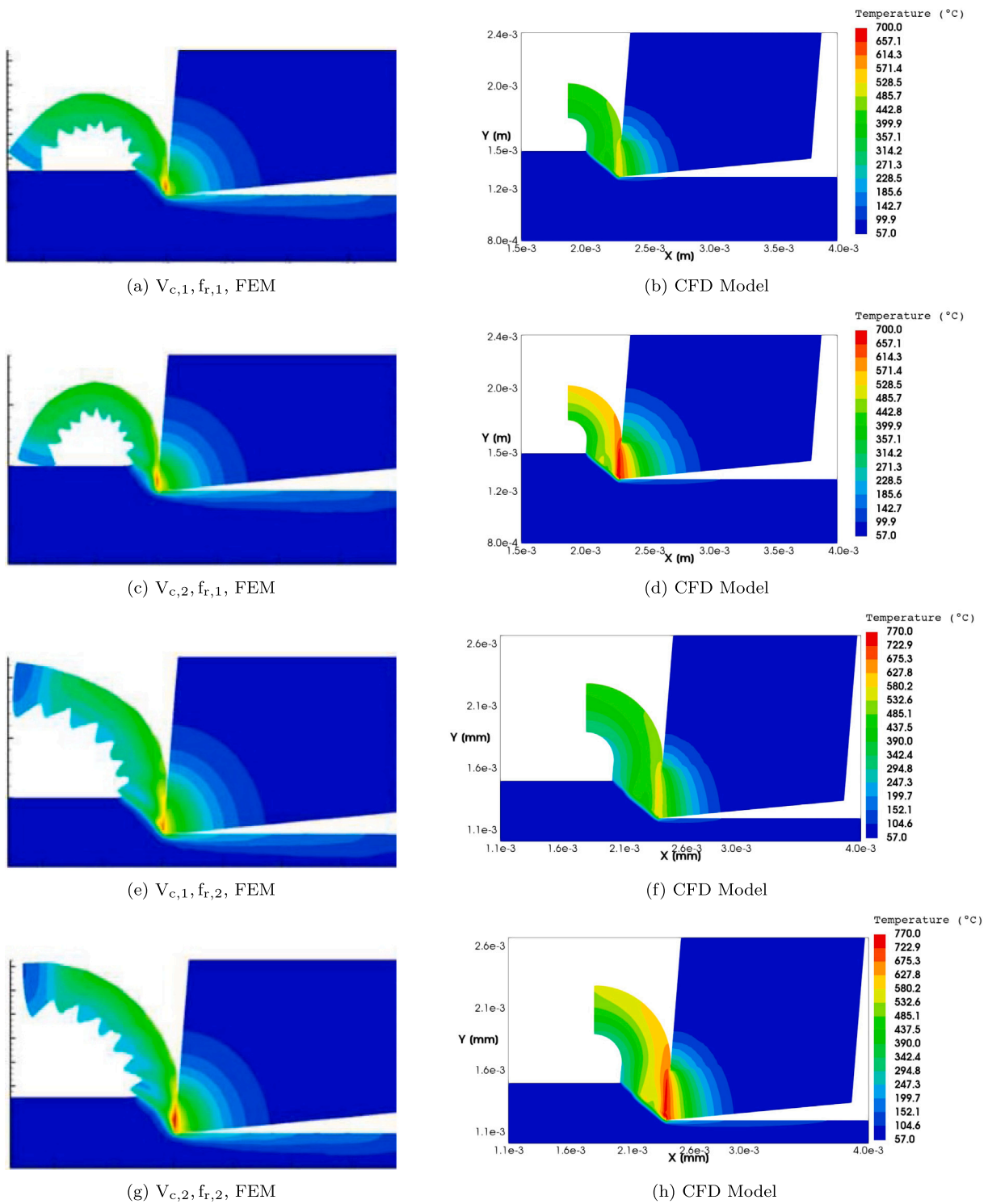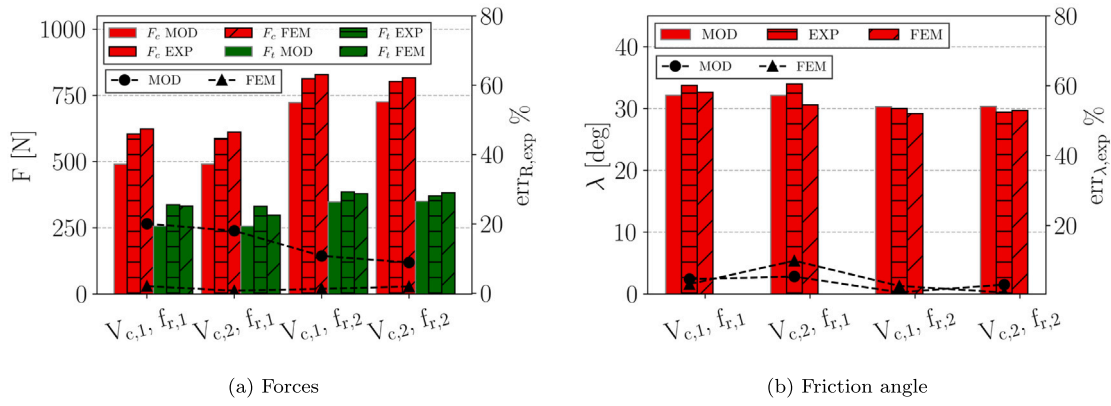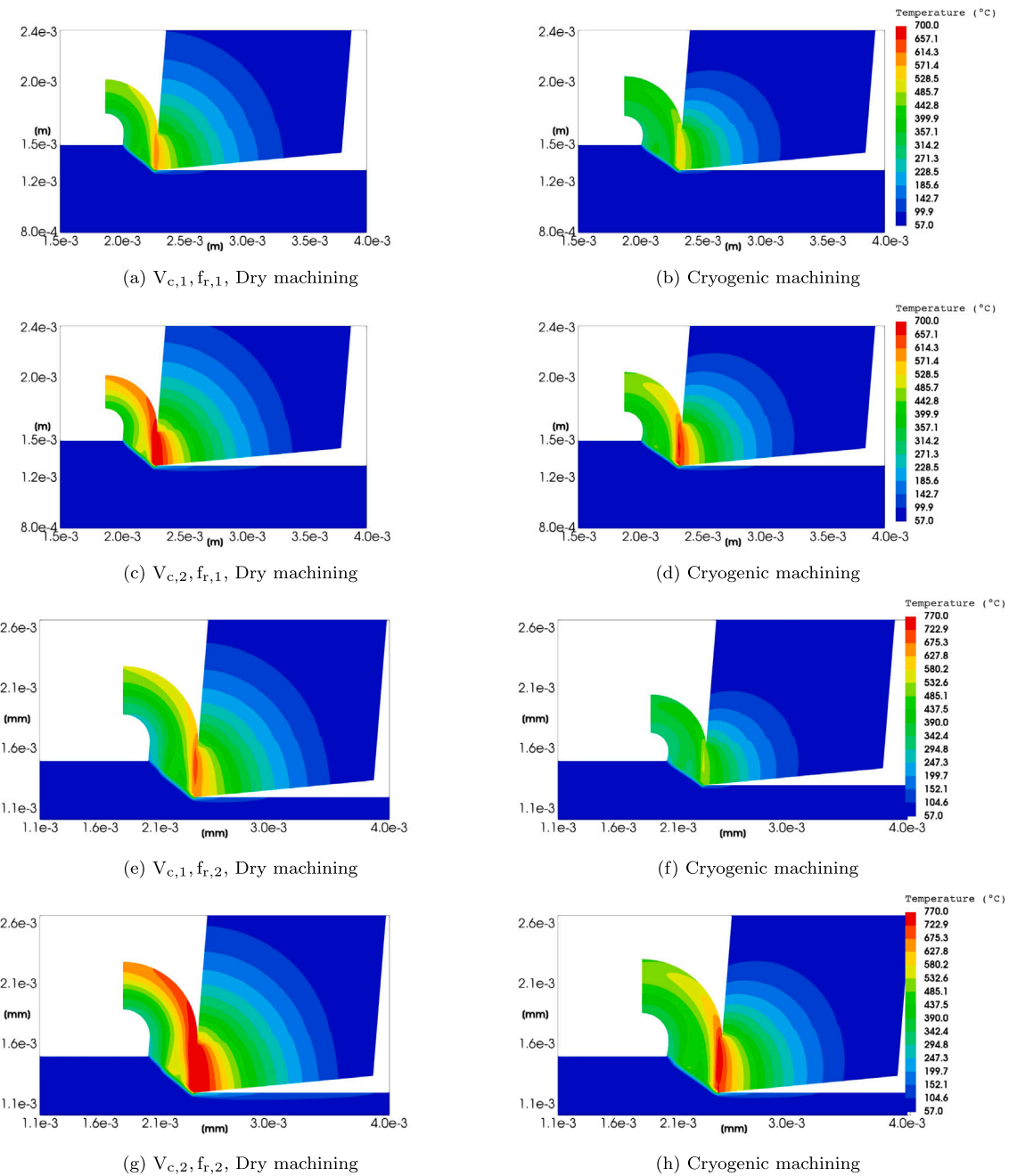(e) $V_{c,1}, f_{r,2}$, FEM

(f) CFD Model

(g) $V_{c,2}, f_{r,2}$, FEM

(h) CFD Model

Fig. 9. Thermal map for different dry Ti4Al6Av cutting conditions: numerical vs FEM prediction.

(a) Forces

(b) Friction angle

Fig. 10. Cutting and Thrust forces and friction angle for cryogenic cutting conditions: numerical prediction vs experimental measurements vs FEM prediction.

(a) $V_{c,1}, f_{r,1}$, Dry machining

(b) Cryogenic machining

(c) $V_{c,2}, f_{r,1}$, Dry machining

(d) Cryogenic machining

(e) $V_{c,1}, f_{r,2}$, Dry machining

(f) Cryogenic machining

(g) $V_{c,2}, f_{r,2}$, Dry machining

(h) Cryogenic machining

Fig. 11. Temperature Map: dry vs cryogenic prediction for Ti4Al6V cutting cases.

3.3. Cryogenic cooling imposing the HTC

The value of the HTC coefficient for LN2 impingement for cryogenic machining was estimated by different authors. Hong et al. [33] proposed a value between 23.27 and 46.75 kW/(m²K), depending on the operating condition. Pusavec estimated a value of 20 kW/(m²K) for the fully developed Leidenfrost regime ($T_{overheat} > 200$ K). The Pusavec estimation has been employed in this study for the rake face. The effectiveness of the cooling on the flank face was discussed with the authors of the reference paper. It can be noted by the photos available of the tool that the jet does not seem to impact the flank face (quote C in Fig. 5). It is hence plausible a reduction of the cooling effectiveness in this area. For this reason, the value of the heat transfer imposed on this surface is assumed as half of the Pusavec estimation, so 10 kW/(m²K). Table 3 shows the resulting reduction of the temperature in the deformation zones. The SSZ is characterized by a higher decrease in

Table 3
Cryogenic temperature reduction in primary and secondary deformation zones.

	$\Delta T_{cryo,PSZ}$ [K]	$\Delta T_{cryo,SSZ}$ [K]
$V_{c,1}, f_{r,1}$	1.67	37.58
$V_{c,2}, f_{r,1}$	1.93	41.6
$V_{c,1}, f_{r,2}$	1.3	36.1
$V_{c,2}, f_{r,2}$	1.7	42.04

temperature since it is closer to the application of the cooling. Fig. 10 shows the comparison between the simulated and experimental forces in cryogenic machining.

Fig. 11 shows the temperature difference between dry and cryogenic cases for the different cutting conditions.
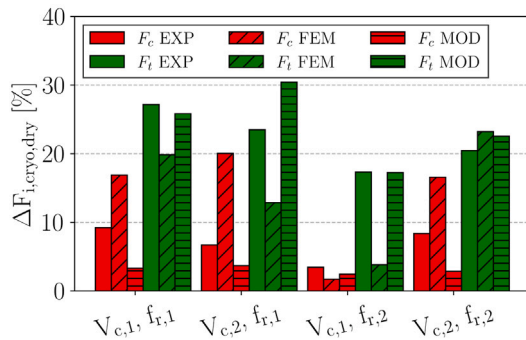

Fig. 12. Cutting and Thrust force increase in cryogenic case for numerical predictions and experimental measurements.

Fig. 12 shows the comparison between dry and cryogenic cutting for numerical and experimental predictions. The variation of the forces

between cryogenic and dry conditions is defined as follows:

$$\Delta F_{i,cryo,dry} = \frac{F_{i,cryo} - F_{i,dry}}{F_{i,dry}}. \tag{29}$$

It is clear the effect of the cooling both on the chip and the tool. The effect of the temperature correction on the cutting model is a rise of both the cutting and the thrust force since the softening of the material is reduced. The experimental data show a higher increase in the thrust forces than the cutting forces. The magnitude of the increase of the thrust force is very close to the experimental results for the majority of the cases, while the increase of the cutting force tends to be underestimated. The FEM analysis prescribes a different behaviour since the magnitude of the increase of thrust and cutting forces is comparable.

3.4. Cryogenic cooling with spray modelling

This section shows the potentiality of the application of spray modelling to cryogenic machining. The heat transfer characteristics of a hypothetical cooling system are determined and the model is run to estimate the forces for a single operating condition ($V_{c,1}, f_{r,1}$). The average surface heat transfer resultant from the post-processing of the spray impingement case was also used to initialize a second simulation without the spray modelling to study the effect of the heat transfer non-uniformity on the cutting forces.

The operating conditions of the jet must be defined to simulate the spray. The injection point and the spray direction were set on the plane of symmetry, to preserve a planar condition. The diameter of the nozzle was set equal to 1 mm, while the injection pressure was set to 2 bar, for a mass flow rate of 0.33 l/min. The jet of nitrogen undergoes flash boiling break up immediately after the evacuation from the nozzle. It causes the formation of droplets with a much smaller diameter and a drop in the temperature to the saturation point of nitrogen, as highlighted in Fig. 13(a). The temperature decrease is justified by the vaporization mechanism: super-heat vaporization is not driven by heat transfer with the environment, it follows that to conserve the droplet's internal energy a decrease of mass must be followed by a decrease of temperature. From the modelling point of view, this behaviour is satisfied by the vaporization rate definition, since it is the combination of a contribution driven by heat transfer and a second one driven by flash boiling (Section 2.5). Furthermore, the evaporation cools down the air (spray cooling). Hence, the enhanced cooling of the cutting area is due both to the direct cooling caused by the droplet impact and to the higher convective cooling due to the higher temperature difference between the metal and the air. During the impingement the heat is exchanged between the wall and the droplets. Since cryogenic droplets are in a saturated state before the impact, the heat absorbed does not
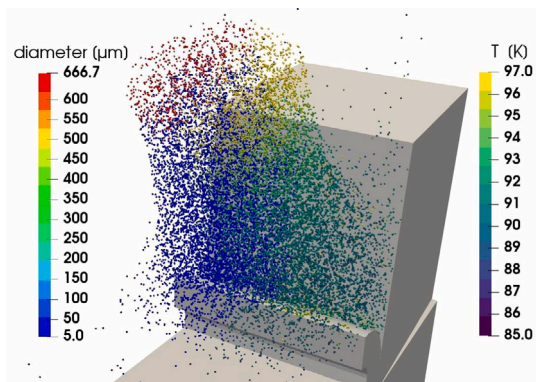
(a) Graphical representation of the cryogenic spray properties
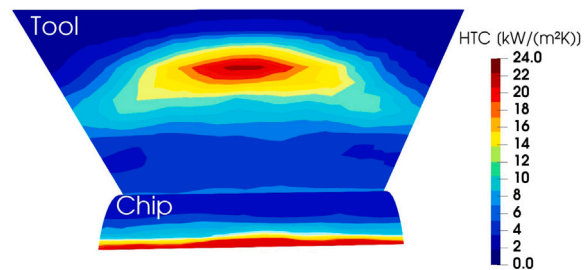
(b) Cryogenic cooling Heat Transfer

Fig. 13. Spray impingement representation (40 m/min, 0.2 mm)

cause an increase of the temperature but further evaporation and thus a reduction of mass.

The heat transfer map on the rake of the tool and the surface of the chip is shown in Fig. 13(b). The average heat transfer coefficients are 15 kW/(m²K) on the tool and 10 kW/(m²K) on the chip surface, these values are close to literature experimental estimations (Hong et al. 23.27–46.75 kW/(m²K), Pusavec 20 kW/(m²K) [14,33]). The underestimation can be explained by a different mass flow rate of the spray and by different operating conditions. Fig. 14 shows the distribution of the HT on the chip and tool surfaces, the non-uniformity of the heat transfer is evident. A region not interested in the spray impact is present on both surfaces. Here the heat transfer mechanism is convection with air. The points above this base heat transfer are characterized by spray impact. The maximum values are in correspondence with a lower surface temperature. Here the impact direction tends to be orthogonal with the surface, maximizing the impact momentum and thus the droplet heat transfer. Note that these points are far from the cutting edge Fig. 13(b).
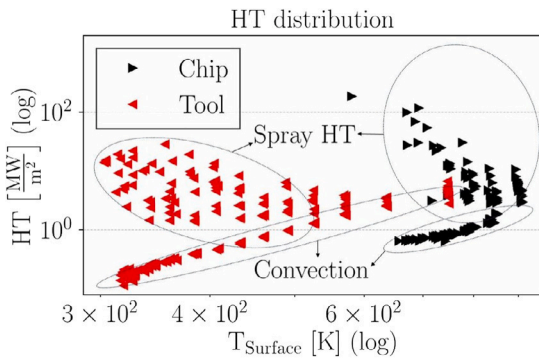

Fig. 14. Heat Transfer distribution.

The temperature of the deformation zones in the spray modelling case is 578 K for the PSZ and 888.75 K for the secondary. The resultant average heat transfers on the rake and chip surfaces are used to initialize a simulation with the simplified approach. Applying for the average heat transfer the resultant temperature is 578 K for the primary and 887.6 K for the secondary. The differences are minimal hence the effect on the forces.

3.5. Computational cost

This section presents the comparison of the computational time among the different simulation approaches. The most expensive process is the CHT simulation. In the first loop, the dry and cryogenic ones are run in parallel, and the computational cost is hence the slower simulation. Table 4 compares the two approaches, it is clear that the higher accuracy deriving by the spray modelling is achieved at the cost of an increase of the computational time of 70 times.

Table 4
Computational costs.

	Analytic mod.	CFD prep.	CFD sim
$t \left[\frac{min}{proc} \right]$	0.1	2	35 (Dry) 5 (cryo impos.) 1440 (cryo spray)

Furthermore, in the approach with the imposed cryogenic heat transfer, the simulation in dry conditions is the slower, since the air region is there resolved. A simplification could be to impose the heat transfer coefficient in the dry case. In this hypothesis, the overall computational time would be close to 10 min.

4. Conclusions

This study presents a simulation approach for cryogenic orthogonal cutting based on the integration of an analytical cutting model and

CFD simulations. The analytical cutting model proposed by Bai [16] for Ti6Al4V interacts with cutting CHT simulations to estimate the forces, the chip geometry and the temperature map of the cutting region both for dry and cryogenic cutting. The cryogenic cooling is treated both by imposing the heat transfer coefficients on the solid surfaces and by modelling the spray and the spray impingement.

The approach was tested against literature experimental data and FEM simulations [7] for different cutting conditions. It accurately estimates the forces, the geometry and the thermal map for all the tested conditions. Furthermore, it proved to correctly capture the effect of cryogenic cooling on the cutting forces. The average error in dry cutting is 11.85% and 14.4% in cryogenic conditions. The computational time of these simulations is close to 41 min for the overall process. They are therefore particularly useful for design purposes and could be integrated into an optimization algorithm. The detailed simulation of the spray impingement was used to define the heat transfer characteristics of a cooling system. The results show that the heat transfer map on the tool and chip surfaces is highly non-homogeneous. The traditional methodology to impose a heat transfer coefficient on these surfaces cannot capture this characteristic. However, the effect of this non-uniformity on the temperature in the deformation regions is limited.

The proposed methodology could be extended to study different cutting technologies, for example, milling, and different cooling methodologies, like MQL. Furthermore, the design of the cooling system could be optimized thanks to the information resulting from the detailed cooling simulation.

Funding

Declaration of competing interest

The authors declare that they have no known competing financial interests or personal relationships that could have appeared to influence the work reported in this paper.

References

[1] Damir A, Sadek A, Attia H. Characterization of machinability and environmental impact of cryogenic turning of Ti-6Al-4V. Procedia CIRP 2018;69:893–8. http://dx.doi.org/10.1016/j.procir.2017.11.070, URL https://www.sciencedirect.com/science/article/pii/S2212827117308466 25th CIRP Life Cycle Engineering (LCE) Conference, 30 April – 2 May 2018, Copenhagen, Denmark.

[2] Li J, Zuo Y, Wang Y, Wang Y, Liu H, Zhang J, et al. On the chip formation mechanism when cutting Ti6Al4V with localised supply of liquid nitrogen. J Mater Process Technol 2024;118377. http://dx.doi.org/10.1016/j.jmatprotec.2024.118377, URL https://www.sciencedirect.com/science/article/pii/S0924013624000955.

[3] Shokrani A, Dhokia V, Muñoz-Escalona P, Newman S. State-of-the-art cryogenic machining and processing. Int J Comput Integr Manuf 2013;26(7):616–48. http://dx.doi.org/10.1080/0951192X.2012.749531.

[4] Albertelli P, Strano M, Monno M. Simulation of the effects of cryogenic liquid nitrogen jets in Ti6Al4V milling. J Manuf Process 2023;85:323–44. http://dx.doi.org/10.1016/j.jmapro.2022.11.053, URL https://www.sciencedirect.com/science/article/pii/S1526612522008325.

[5] Pereira O, Celaya A, Urbikaín G, Rodríguez A, Fernández-Valdivielso A, de Lacalle LNL. CO2 cryogenic milling of inconel 718: cutting forces and tool wear. J Mater Res Technol 2020;9(4):8459–68. http://dx.doi.org/10.1016/j.jmrt.2020.05.118, URL https://www.sciencedirect.com/science/article/pii/S2238785420313879.

[6] Nalbant M, Yildiz Y. Effect of cryogenic cooling in milling process of AISI 304 stainless steel. Trans Nonferr Met Soc China 2011;21(1):72–9. http://dx.doi.org/10.1016/S1003-6326(11)60680-8, URL https://www.sciencedirect.com/science/article/pii/S1003632611606808.

[7] Davoudinejad A, Chiappini E, Tirelli S, Annoni M, Strano M. Finite element simulation and validation of chip formation and cutting forces in dry and cryogenic cutting of Ti–6Al–4V. Procedia Manuf 2015;1:728–39. http://dx.doi.org/10.1016/j.promfg.2015.09.037, URL https://www.sciencedirect.com/science/article/pii/S2351978915010379 43rd North American Manufacturing Research Conference, NAMRC 43, 8-12 June 2015, UNC Charlotte, North Carolina, United States.

[8] Pušavec F, Grguraš D, Koch M, Krajnik P. Cooling capability of liquid nitrogen and carbon dioxide in cryogenic milling. CIRP Ann 2019;68(1):73–6. http://dx.doi.org/10.1016/j.cirp.2019.03.016, URL https://www.sciencedirect.com/science/article/pii/S0007850619300174.

[9] Lequien P, Poulachon G, Outeiro J, Rech J. Hybrid experimental/modelling methodology for identifying the convective heat transfer coefficient in cryogenic assisted machining. Appl Therm Eng 2018;128:500–7. http://dx.doi.org/10.1016/j.applthermaleng.2017.09.054, URL https://www.sciencedirect.com/science/article/pii/S1359431117326972.

[10] Golda P, Lettner N, Schießl R, Maas U. Experimental investigation of the cryogenic LN2-cooling performance for an impinging jet configuration for different inflow conditions. Int J Heat Mass Transfer 2021;180:121776. http://dx.doi.org/10.1016/j.ijheatmasstransfer.2021.121776, URL https://www.sciencedirect.com/science/article/pii/S0017931021008814.

[11] Salame C, Bejjani R, Marimuthu P. A better understanding of cryogenic machining using CFD and FEM simulation. Procedia CIRP 2019;81:1071–6. http://dx.doi.org/10.1016/j.procir.2019.03.255, URL https://www.sciencedirect.com/science/article/pii/S2212827119305608 52nd CIRP Conference on Manufacturing Systems (CMS), Ljubljana, Slovenia, June 12-14, 2019.

[12] Tahmasebi E, Albertelli P, Lucchini T, Monno M, Mussi V. CFD and experimental analysis of the coolant flow in cryogenic milling. Int J Mach Tools Manuf 2019;140:20–33. http://dx.doi.org/10.1016/j.ijmachtools.2019.02.003, URL https://www.sciencedirect.com/science/article/pii/S0890695518306606.

[13] Kim D, Kim D, Park H. Numerical and experimental study of end-milling process of titanium alloy with a cryogenic internal coolant supply. Int J Adv Manuf Technol 2019;105. http://dx.doi.org/10.1007/s00170-019-04425-3.

[14] Pusavec F, Lu T, Courbon C, Rech J, Aljancic U, Kopac J, et al. Analysis of the influence of nitrogen phase and surface heat transfer coefficient on cryogenic machining performance. J Mater Process Technol 2016;233:19–28. http://dx.doi.org/10.1016/j.jmatprotec.2016.02.003, URL https://www.sciencedirect.com/science/article/pii/S092401361630036X.

[15] Lalwani D, Mehta N, Jain P. Extension of Oxley's predictive machining theory for Johnson and Cook flow stress model. J Mater Process Technol 2009;209(12):5305–12. http://dx.doi.org/10.1016/j.jmatprotec.2009.03.020, URL https://www.sciencedirect.com/science/article/pii/S0924013609001101.

[16] Bai W, Sun R, Roy A, Silberschmidt VV. Improved analytical prediction of chip formation in orthogonal cutting of titanium alloy Ti6Al4V. Int J Mech Sci 2017;133:357–67. http://dx.doi.org/10.1016/j.ijmecsci.2017.08.054, URL https://www.sciencedirect.com/science/article/pii/S0020740317310330.

[17] Berlemont A, Desjonqueres P, Gouesbet G. Particle lagrangian simulation in turbulent flows. Int J Multiph Flow 1990;16(1):19–34. http://dx.doi.org/10.1016/0301-9322(90)90034-G, URL https://www.sciencedirect.com/science/article/pii/030193229090034G.

[18] Oxley PLB, Shaw MC. Mechanics of machining: an analytical approach to assessing machinability. In: Proceedings of the Twenty-second International Machine Tool Design and Research Conference. 1990, URL https://link.springer.com/chapter/10.1007/978-1-349-06281-2_35.

[19] Binglin Li YH, Li C. Analytical prediction of cutting forces in orthogonal cutting using unequal division shear-zone model. Int J Adv Manuf Technol 2011;54:431–43. http://dx.doi.org/10.1007/s00170-010-2940-8, URL https://link.springer.com/article/10.1007/s00170-010-2940-8.

[20] Boothroyd G. Temperatures in orthogonal metal cutting. Proc Inst Mech Eng 1963;177(1):789–810. http://dx.doi.org/10.1243/PIME_PROC_1963_177_058_02, URL https://journals.sagepub.com/doi/10.1243/PIME_PROC_1963_177_058_02.

[21] Kim DY, Kim DM, Park HW. Numerical and experimental study of end-milling process of titanium alloy with a cryogenic internal coolant supply. Int J Adv Manuf Technol 2019;105. http://dx.doi.org/10.1007/s00170-019-04425-3, URL https://link.springer.com/article/10.1007/s00170-019-04425-3.

[22] Horne JG. A new model for initial chip curl in continuous cutting. Int J Mech Sci 1978;20(11):739–45. http://dx.doi.org/10.1016/0020-7403(78)90095-4, URL https://www.sciencedirect.com/science/article/pii/0020740378900954.

[23] Carroll JT, Strenkowski JS. Finite element models of orthogonal cutting with application to single point diamond turning. Int J Mech Sci 1988;30(12):899–920. http://dx.doi.org/10.1016/0020-7403(88)90073-2, URL https://www.sciencedirect.com/science/article/pii/0020740388900732.

[24] Zienkiewicz O, Jain P, Onate E. Flow of solids during forming and extrusion: Some aspects of numerical solutions. Int J Solids Struct 1978;14(1):15–38. http://dx.doi.org/10.1016/0020-7683(78)90062-8, URL https://www.sciencedirect.com/science/article/pii/0020768378900628.

[25] He L, Oldfield MLG. Unsteady conjugate heat transfer modeling. J Turbomachinery 2010;133(3). http://dx.doi.org/10.1115/1.4001245.

[26] Ahrens JP, Geveci B, Law CC. ParaView: An end-user tool for large-data visualization. In: The visualization handbook. 2005, http://dx.doi.org/10.1016/B978-012387582-2/50038-1, URL https://api.semanticscholar.org/CorpusID:56558637.

[27] Leidenfrost JG. On the fixation of water in diverse fire. Int J Heat Mass Transfer 1966;9(11):1153–66. http://dx.doi.org/10.1016/0017-9310(66)90111-6, URL https://www.sciencedirect.com/science/article/pii/0017931066901116.

[28] Duronio F, Ranieri S, Montanaro A, Allocca L, De Vita A. ECN spray G injector: Numerical modelling of flash-boiling breakup and spray collapse. Int J Multiph Flow 2021;145:103817. http://dx.doi.org/10.1016/j.ijmultiphaseflow.2021.103817, URL https://www.sciencedirect.com/science/article/pii/S0301932221002470.

[29] Zuo B, Gomes A, Rutland C. Modeling superheated fuel spray and vaporization. Int J Engine Res 2000;1:321–36. http://dx.doi.org/10.1243/1468087001545218, URL https://journals.sagepub.com/doi/10.1243/1468087001545218.

[30] Kuhnke D. Spray/wall-interaction modelling by dimensionless data analysis. Shaker; 2004, URL https://tubiblio.ulb.tu-darmstadt.de/22954/.

[31] Deb S, Yao SC. Analysis on film boiling heat transfer of impacting sprays. Int J Heat Mass Transfer 1989;32(11):2099–112. http://dx.doi.org/10.1016/0017-9310(89)90117-8, URL https://www.sciencedirect.com/science/article/pii/0017931089901178.

[32] Moufki A, Molinari A, Dudzinski D. Modelling of orthogonal cutting with a temperature dependent friction law. J Mech Phys Solids 1998;46(10):2103–38. http://dx.doi.org/10.1016/S0022-5096(98)00032-5, URL https://www.sciencedirect.com/science/article/pii/S0022509698000325.

[33] Hong SY, Ding Y. Cooling approaches and cutting temperatures in cryogenic machining of Ti-6Al-4V. Int J Mach Tools Manuf 2001;41(10):1417–37. http://dx.doi.org/10.1016/S0890-6955(01)00026-8, URL https://www.sciencedirect.com/science/article/pii/S0890695501000268.